Full-PIC Simulation of an ECR Plasma Thruster with Magnetic Nozzle

Jean C. Porto, Paul-Quentin Elias

Full-PIC Simulation of an ECR Plasma Thruster with Magnetic Nozzle

Jean C. Porto[*] and Paul-Quentin Elias[†]

ONERA-The French Aerospace Lab, Université Paris Saclay, F-91123 Palaiseau – France

Abstract: A coaxial ECR thruster is simulated using a 1D3V electromagnetic Particle-In-Cell code coupled to a Monte-Carlo Collision module. The goal is to get a better understanding of the physical behavior of the thruster, in particular the wave absorption mechanism. For this purpose a non-dissipative wave solver is used, based on the Linear Bicharacteristic Scheme. The PIC model is used to run a parametric analysis of some simulation factors. The tendencies found in the simulation are in line with previous experimental results. This tools will be used to improve our understanding of the basic phenomena in the thruster and guide future modeling effort in 2D and 3D.

Nomenclature

ECR	= Electron Cyclotron Resonance
PIC	= Particle-In-Cell
MCC	= Monte-Carlo Collision
CFL	= Courant-Friedrichs-Lewy condition
$EEDF$	= Electron Energy Distribution Function

I.   Introduction

SPACE exploration, either for scientific purposes or for its commercial exploitation, heavily depend nowadays on the available electric thruster technologies. This type of propulsion system experienced a significant improvement since their first developments in the 1960s, and they are currently a mature technology. Their efficient utilization of the propellant mass provide remarkable gains in term of payload and lifetime.

Among the most well-known electric propulsion technologies we found the Grided Ion Engine or the Hall Effect Thruster. Their working principle is based on an electrostatic acceleration of a beam of ions which have to be neutralized after leaving the ionization chamber. However, this kind of configuration presents some limitations related to its performances and lifetime which could be improved with optimized or new electric thrusters such as Magnetically Shielded Hall Thrusters or Double Stage Hall Effect Thrusters.[1,2] This represents an active research area since the space industry have been experiencing an important growth in the past several years thanks to new actors in the fields of telecommunications, navigation systems, scientific missions, and even human spaceflight. According to Eurospace (the association of the European Space Industry) in his *Space Trends* released in 2015, between 2005 and 2014 the number of launches around the world increased by 70%.[3] This growing trend needs to be fulfill with new technologies capable of meeting the challenges of the future by achieving higher performances.

---

[*]PhD Student, Physics - Instrumentation and Space Department, jean_carlos.porto_hernandez@onera.fr
[†]Research Scientist, Physics - Instrumentation and Space Department, paul-quentin.elias@onera.fr

For this purpose, in the framework of the European Union's Horizon 2020 research and innovation program, the project MINOTOR is trying to demonstrate the feasibility of a new propulsion device. The concept consist on a cathode-less and grid-less plasma thruster called ECRA (Electron Cyclotron Resonance Accelerator) under development at Onera.[4,5] It is composed of a coaxial chamber where a quasi-neutral plasma is confined and guided using a diverging magnetic field (see Fig. 1). Thanks to the cyclotron resonance phenomenon, the electrons are heated up by electromagnetic waves from a micro-wave generator at 2.45 GHz. The magnetic field is set in order to reach the resonance condition for the electrons at what we call the "ECR surface" (equality of the electron cyclotron frequency and the exciting one of the microwaves at B = 87.5 mT).

Various experimental investigations have characterized the thruster performances and optimized its efficiency.[7–10] However, the complex physics inside the thruster is not yet fully understood. To tackle this problem, advanced numerical codes are developed to model its behavior and get a better understanding of several phenomena taking place within the plasma source.[11,12] Among the key issues to understand we can find the anisotropic microwave heating by resonant absorption, the non-local transport of magnetized electrons (mean free path greater than the source radius), and the effect of the coaxial chamber walls in the thruster performance by potentially altering the confinement mode of the plasma. The Particle-In-Cell (PIC) method is a good candidate to give us a detailed description of these kinetic and non-local effects: electrons dynamics inside the source, microwave energy transfer and the plasma-walls interaction.

Figure 1. Schematic view of the ECRA thruster under development at Onera.[6]

PIC methods have already been used to simulate low-temperature plasmas inside electric propulsion devices, including gridded RF thruster.[13,14] However, to our knowledge, none of these published works described the same type of gridless configuration as the ECRA with a magnetic nozzle.

A previous work carried out at Onera and presented in Ref. 11 helped us to get some insight into the plasma physics within the coaxial chamber. It used a simplified 1.5D model described as 1D3V (one-dimensional in space and three-dimensional in velocity). However, it did not take into account the self-consistent electromagnetic wave propagation through the plasma. The objective of this work is to simulate this model adding an electromagnetic module to get a better description of the microwave propagation and a deeper understanding of the physics phenomena taking place. We will limit our study to this quasi-one-dimensional model to focus ourselves on all the new knowledge we could get with this simplified approach. After that, it will be used to guide the next steps in the thruster simulation in higher dimensions.

To achieve this goal, the implementation of the electromagnetic solver is required to model the wave propagation within the plasma source. In order to build an accurate solver, the Linear Bicharacteristic Scheme (LBS) was chosen for the one-dimensional configuration. An asset of this method is its lack of numerical dissipation, its low numerical dispersion, and its simplicity to treat the outer boundary conditions via the Perfectly Matched Layer (PML) concept.[15] This feature is helpful to take into account the absorbing boundary condition at the thruster outlet. The Maxwell solver is integrated in Onera's PIC code coupled to a Monte-Carlo Collision module (MCC) and adapted to massively parallel architectures. The code can be run with either a pure MPI or a hybrid MPI/OpenMP parallelization.

In conclusion, this work will present the full-PIC modeling of the ECRA thruster. First, the main characteristic of the Oneras PIC/MCC code will be briefly described. Particular interest will be paid to the implemented Maxwell solver. Second, using the simplified kinetic model, an analysis of the thruster response to the variation of some of the simulation parameters will be done.
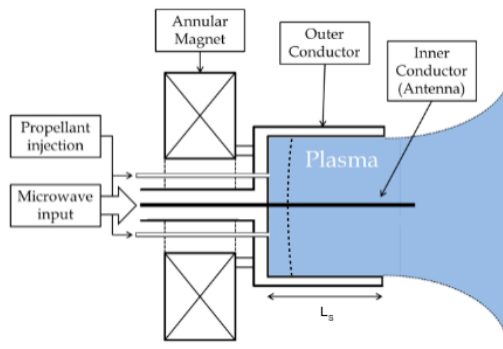
II. Numerical model of the thruster

A. Model overview

The main characteristics of the 1D3V kinetic model are:

a) Creation and expansion of a plasma in a magnetic field tube (see Fig. 2)

b) All the plasma properties are considered constant along the section of the magnetic field tube but vary along its axis

c) The electrons and the ions are assumed to be confined within the magnetic field tube, whose area is related to the axial magnetic field intensity through:

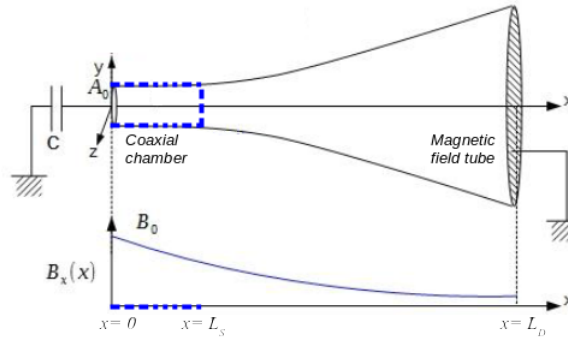$$\frac{A(x)}{A_0} = \frac{B_0}{B_x(x)} \tag{1}$$

Figure 2. Simplified quasi-one-dimensional model of the thruster.

The magnetic field follows an exponentially decaying profile varying as a function of a characteristic length L_B. Its maximum value (B_0) is reached at x = 0 mm. The position and the velocity of each charged particle will be updated with the following equations of motion:

$$m\frac{\mathrm{d}\vec{v}}{\mathrm{d}t} = q\left[\vec{E}_{ES} + \vec{E}_{EM} + \vec{v} \times \left(\vec{B}_{MS} + \vec{B}_{EM}\right)\right] \quad and \quad \frac{\mathrm{d}\vec{x}}{\mathrm{d}t} = \vec{v} \tag{2}$$

Where q is the charge of the particle, m the mass, $\vec{x}$ the position and $\vec{v}$ the velocity. $\vec{E}_{ES}$ is the electrostatic field generated by the charge distribution. $\vec{B}_{MS}$ is the magnetostatic field generated by permanents magnets. Finally, $\vec{E}_{EM}$ and $\vec{B}_{EM}$ are the result of the electromagnetic field produced by the microwave source. There are several numerical schemes to integrate these equations of motion, such as Runge-Kutta or the leap-frog method. The last option is commonly used since it requires a smaller number of mathematical operations and a lower storage capability in comparison with more complex alternatives.[16] This solution is coupled to a Boris scheme algorithm to get the $\vec{v} \times \vec{B}$ rotation resulting from the Lorentz force.

To compute the electrostatic contribution to the electric field from the charge and current distribution, a Poisson solver is used. Under the assumption that the electrostatic part of the electric field id aligned with the magnetostatic field, and taking into account the relationship given in Eq. 1, the Poisson equation to be solved is as follows:

$$\epsilon_0 \frac{\partial}{\partial x}\left(\frac{B_0}{B(x)}E_x\right) = \frac{B_0}{B(x)}\rho \tag{3}$$

The collisions of the particles against a neutral background are modeled using a Monte-Carlo Collision (MCC) module. Its done by adding an extra step in the PIC loop to find those particles that undergo a collision. The module uses the *Null Collision* technique[17] to simplify the computation of the collision test by removing the velocity dependency in the cross-section through the introduction of $\sigma_{max} = \max[\sigma(v)]$.

In the thruster, the neutral gas is injected at the backplate. This gas expands in the source and then in the vacuum chamber, resulting in a decrease of the number density. In this work this is modeled by assuming that the background number density follows and exponential profile:

$$n(x) = n_0 \exp\left(-\frac{x}{L_n}\right) \tag{4}$$

Note the we do not take into account the neutral gas depletion.

Finally, the particle losses across the magnetic field tubes is modeled by a phenomenological volume loss model that computes the diffusion rate across the magnetic field lines of the electron guiding centers. This diffusion is due to elastic collisions in the classical limit. This diffusion rate can be enhanced to model anomalous diffusion with a parameter. The magnitude of the losses is important to control the electron temperature. For the sake of this discussion the loss model is tuned to provide potential profile close to the experimental one and left unchanged for the rest of the parametric study.

B. Electromagnetic field solver

To build the full-PIC simulation we need to develop an electromagnetic module to simulate the microwave propagation through the computational domain. A brief description of the implemented numerical scheme (Linear Bicharacteristic Scheme or also known as Upwind Leapfrog Method) is presented below.

First of all, we start with the Maxwell-Faraday and Maxwell-Ampère equations for a lossy media on the 1D configuration ($\partial/\partial y = \partial/\partial z = 0$) taking into account the relationships $\vec{D} = \epsilon\vec{E}$ and $\vec{B} = \mu\vec{H}$:

$$\vec{\nabla} \times \vec{E} = -\frac{\partial\vec{B}}{\partial t} - \frac{\sigma^*}{\mu}\vec{B},$$
$$\vec{\nabla} \times \vec{B} = \mu\vec{J} + \mu\epsilon\frac{\partial\vec{E}}{\partial t} + \mu\sigma\vec{E}. \tag{5}$$

Where σ and σ^* are the electric and magnetic conductivity, respectively. The equations are recast as:

$$\frac{\partial D_y}{\partial t} + \frac{\partial H_z}{\partial x} + \frac{\sigma}{\epsilon}D_y + J_y = 0 \tag{6}$$

$$\frac{1}{c^2}\frac{\partial H_z}{\partial t} + \frac{\partial D_y}{\partial x} + \frac{\sigma^*}{\mu c}H_z = 0 \tag{7}$$

$$\frac{\partial D_z}{\partial t} - \frac{\partial H_y}{\partial x} + \frac{\sigma}{\epsilon}D_z + J_z = 0 \tag{8}$$

$$\frac{1}{c^2}\frac{\partial H_y}{\partial t} - \frac{\partial D_z}{\partial x} + \frac{\sigma^*}{\mu c}H_y = 0 \tag{9}$$

For the sake of simplicity, further algebraic manipulation will only be presented for the assumption of a current J_y acting as a source term. It means that only Eq. 6 and 7 will be used to solve for D_y and H_z.

The next step towards the construction of the Linear Bicharacteristic Scheme (LBS) scheme is to transform these equations into what is called the "characteristic form", in which each variable will represent a propagating wave over an specific direction or path. In order to do so, we multiply Eq. 7 for the speed of light (c) and then add and subtract it from Eq. 6.

$$\frac{\partial}{\partial t}\left(D_y \pm \frac{1}{c}H_z\right) \pm c\frac{\partial}{\partial x}\left(D_y \pm \frac{1}{c}H_z\right) + \frac{\sigma}{\epsilon}D_y + \frac{\sigma^*}{\mu}H_z + J_y = 0 \tag{10}$$

The characteristic variables can now be defined as:

$$P = D_y + \frac{1}{c}H_z \tag{11a}$$

$$Q = D_y - \frac{1}{c}H_z \tag{11b}$$

Finally we get the next set of equations to represent $\pm x$ propagating solutions:

$$\frac{\partial P}{\partial t} + c\frac{\partial P}{\partial x} + \frac{a}{2}P + \frac{b}{2}Q + J_y = 0 \quad \text{(12a)}$$

$$\frac{\partial Q}{\partial t} - c\frac{\partial Q}{\partial x} + \frac{b}{2}P + \frac{a}{2}Q + J_y = 0 \quad \text{(12b)}$$

Where:

$$a = \frac{\sigma}{\epsilon} + \frac{\sigma^*}{\mu} \quad and \quad b = \frac{\sigma}{\epsilon} - \frac{\sigma^*}{\mu} \tag{13}$$

The fourth term of equations 12a and 12b represent what its called the "source term". To develop the discretized equations of the scheme, these terms were treated using the method proposed by Beggs in Ref. 18: indexing the self source term (i.e. P in equation 12a and Q in equation 12b) at time level $n+1$ and the coupled source term (i.e Q in equation 12a and P in equation 12b) at time level n. The advantage of this implementation is to provide a semi-implicit scheme avoiding a matrix solution at each time-step while keeping a good level of accuracy for the numerical solution.

The stencils used for the space-time discretization in the LBS scheme are shown in Fig. 3. This multilevel upwind stencil is compact and clusters the information around each unknown point of the grid. This reduces the required information to be shared among the communicating interfaces of the processors, resulting in a straightforward implementation for parallel codes.[19]
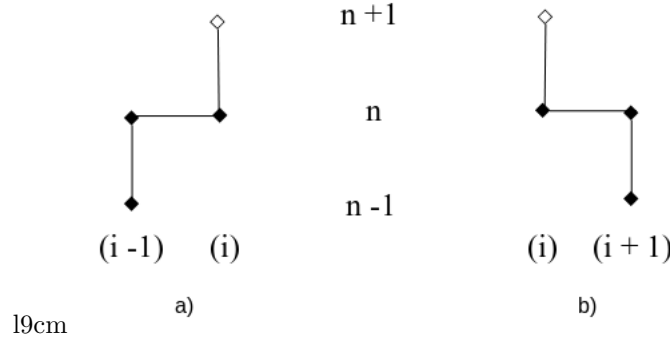

Figure 3. Stencil arrangement: (a) right-going wave +x, and (b) left-going wave -x.

The update equation can finally be written as follows:

$$P_i^{n+1} = \frac{P_{i-1}^{n-1} + (1 - 2\nu)(P_i^n - P_{i-1}^n) - b\Delta t Q_i^n - 2\Delta t J_y}{1 + a\Delta t} \tag{14}$$

$$Q_i^{n+1} = \frac{Q_{i+1}^{n-1} - (1 - 2\nu)(Q_{i+1}^n - Q_i^n) - b\Delta t P_i^n - 2\Delta t J_y}{1 + a\Delta t} \tag{15}$$

Where $\nu = c\Delta t/\Delta x \leq 1$ is the Courant-Friedrichs-Lewy (CFL) condition to ensure the stability of the scheme. Once the update equations are solved at each iteration for P and Q, we can translate back to the original variables D and H using equations 11a and 11b.

C. Boundary conditions

The computational domain goes from $x = 0$ at the left side where the dielectric thruster backplate is located, to $x = L_D$ at the vacuum chamber wall. The open end of the coaxial chamber, known as the plasma source, is represented using the blue dashed line in Fig. 2 at $x = L_S$. The density of neutral particles inside the coaxial chamber is modeled with an exponentially decaying function. We can impose the maximum value at x = 0 mm, n_0, and a characteristic length, L_n.

Electrostatics

At the right end of the computational domain, $x = L_D$, we imposed a zero voltage to simulate the presence of the grounded vacuum chamber wall. Any particle crossing this boundary is removed from the simulation.

The dielectric backplate is in contact with the plasma and therefore its surface voltage V_{BP} is changed as it gets impacted by the charged particles. The evolution of V_{BP} through time is modeled as a capacitor:

$$\Delta V_{BP} = \frac{1}{C}\frac{\Delta Q}{\Delta t} \tag{16}$$

Where ΔQ is the charge deposited at the backplate at each time step, and C is an equivalent capacitance under the assumption that the backplate is in contact with a grounded conductor. The secondary electron emission of the backplate is only taken into account for the ions with a constant coefficient γ_{BP}.

Electromagnetics

The backplate is where the electromagnetic power is injected. The energy comes in the form of linearly polarized electromagnetic waves, specified by its power density per unit area, and with a 2.45 GHz frequency.

With the chosen numerical scheme for the Maxwell solver, a PML can be implemented at the right side boundary to avoid reflections of these electromagnetic waves back to the computational domain once they have reached the end. The simplicity of this implementation, without additional storage or modification of the update equations, is one of the advantages of the chosen numerical scheme for the electromagnetic solver.

To do so, the only requirement is to impose $\epsilon = \epsilon_0, \mu = \mu_0,$ and $\sigma^*/\mu = \sigma/\epsilon$. This is made gradually thanks to space-dependents electric and magnetic conductivity profiles: zero outside the PML region, and linearly increasing inside the PML until the achievement of the required condition at the outer nodes of the domain. In theory, the absorption could also be achieved by just forcing $\sigma^*/\mu = \sigma/\epsilon$ in the last node, but such an abrupt dumping could generate wave oscillations coming back from this boundary.

III. Results

The numerical model of the thruster described in section II was simulated using the electromagnetic PIC/MCC code under development at Onera with the following set of parameters:

Table 1. Simulation parameters.

Parameter	Description	Value
Δt	Time step	0.4 ps
Δx	Mesh spacing	190 µm
ν	CFL condition	0.6
f_{EM}	Microwave frequency	2.45 GHz
L_S	Plasma source length	20 mm
x_{ECR}	ECR surface position	5 mm
L_D	Computational domain length	100 mm
n_0	Maximum number density of neutrals	$2 \times 10^{21}\,\mathrm{m}^{-3}$
L_n	Neutrals density characteristic length	0.5 cm
B_0	Magnetic field at the backplate	1000 G
L_B	Magnetic field characteristic length	4 cm
A_0	Cross-sectional area at the backplate	$1\,\mathrm{cm}^2$
γ_{BP}	Secondary electron emission coefficient	0.2

The simulation was run until it reached a steady state. Figure 4 shows the plasma potential distribution over the whole computational domain. The backplate collects ions to reach a positive steady state potential of around 30 V. The peak of the plasma potential is 58 V and it is reached at 3 mm, not at the ECR surface.

A plasma sheath is formed at the backplate as well as at the vacuum chamber wall. The right side plasma sheath is easily noticeable with a beginning point around 97 mm. The effects of the plasma dynamics in this part of the model are also visible on the right bottom side of Fig. 5. The electron and ion number density profiles show the expected quasi-neutrality violation. Besides these two regions of plasma sheaths, Fig. 5 confirms that the quasi-neutrality is conserved in all the others parts of our model. The maximum density value $(2.5 \times 10^{11}\,\mathrm{cm}^{-3})$ is achieved at 2.5 mm.
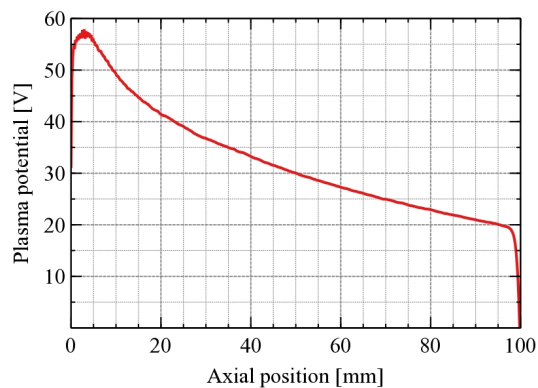
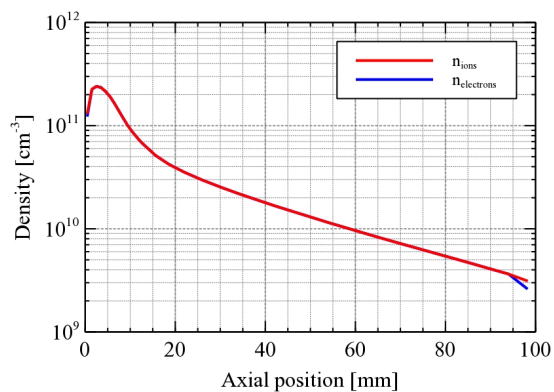**Figure 4. Plasma potential profile.**

Figure 5. Density distribution.

A.   Ion dynamics

To get some insight into the ions dynamics inside the model we can take a look to their velocity distribution function at different locations of the domain in Fig. 6. An artificial ion mass of 1 atomic mass unit was used.
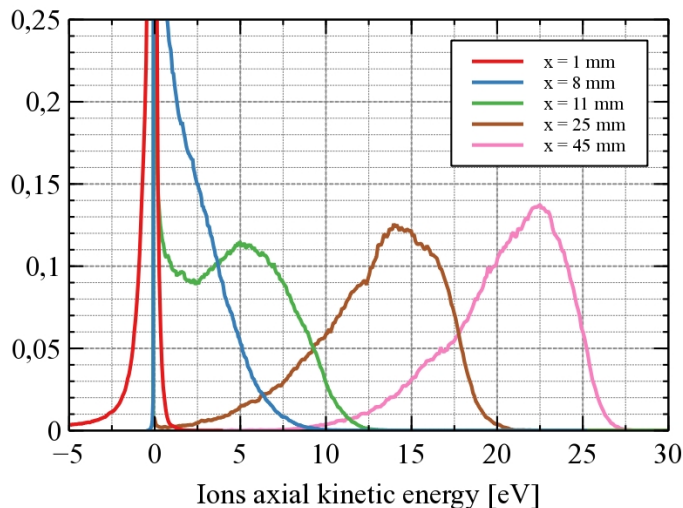

Figure 6. Normalized ion velocity distribution function at different points from the backplate.

The negative energy shown for x = 1 mm represents the direction of the velocity vector. In this region, the vast majority of the ions are moving towards the backplate as a result of the potential well that we saw in Fig. 4. We can notice that for all the remaining points represented in Fig. 6, the mean ion velocity increases as we move away from the plasma source.
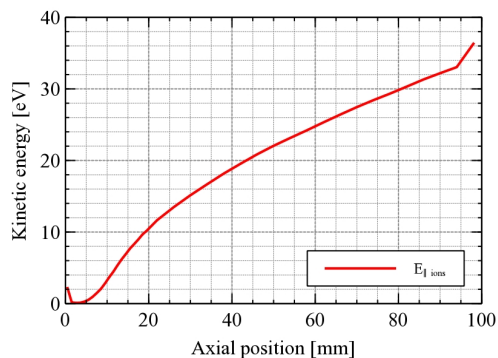

Figure 7. Ion mean kinetic energy.

We can use the ions distribution functions to calculate the mean ion energy profile. The result is shown in Fig. 7. The mean ion kinetic energy for those located close to the vacuum chamber wall does not exceed 40 eV. However, we already saw that the peak plasma potential value was reached at 58 V (around 55 V at x = 5.3 mm), and taking into account that in our PIC/MCC code the ions have almost no energy when they are created, we can infer that the majority of the ions leaving the domain to the right are not created near the ECR surface. In fact, a plasma potential of 40 V is only reached a few millimeters after the end of the source ($L_S = 20$ mm). This suggest that most of the ions are created outside the coaxial chamber.

B. Electron dynamics

The electrons are heated up in the perpendicular direction, gaining energy in their gyromotions around the magnetic field lines. This energy is then used to overcome the electrostatic potential and its also transferred to the electrons axial motion thanks to the divergence of the magnetic field.
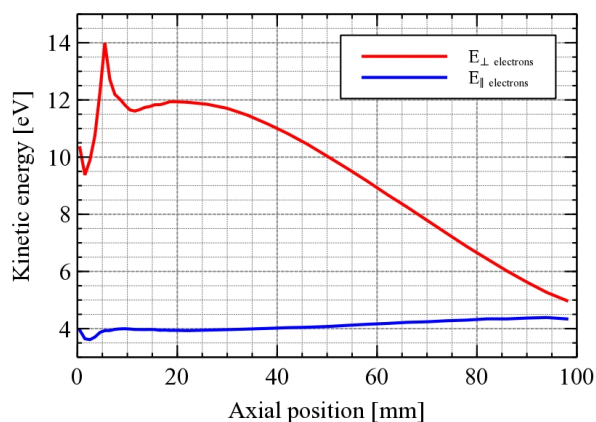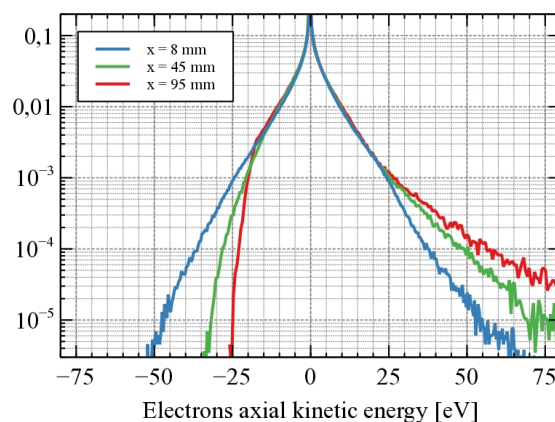

Figure 8. Electrons mean kinetic energy.

Figure 9. EEDF at different positions.

The global maximum electron perpendicular energy is reached at the ECR surface thanks to the resonance condition. Then, this energy decreases before reaching a local maximum value at the end of the plasma source as can be seen in Figure 8. A hypothesis to explain this phenomenon is that it may be the result of a microwave heating taking place in the whole plasma source, and not only in the surroundings of the ECR surface.

After leaving the coaxial chamber, the perpendicular energy becomes a monotonically decreasing function as the longitudinal one increases. Figure 10 shows this energy transfer more clearly with the Electron Energy Distribution Function (EEDF) in both directions.

The electrons behavior inside the plasma source is described by Peterschmitt et al. in Ref. 20 as a bounce motion where they oscillate in an effective potential formed by the converging magnetic field lines close to the backplate, and by the electrostatic field in the other side. The electrons can only leave the thruster once they have reached enough energy to overcome the electrostatic potential barrier. This dynamics can be seen in Fig. 9 where we show the EEDF in the axial direction at three different locations from the backplate: 8 mm, 45 mm, and 95 mm. The negative values of the EEDF represent electrons heading towards the backplate. The symmetric parts of the EEDF around 0 eV represent an equal flux of particles moving away and towards the coaxial chamber, and it describes the oscillating electrons.

As we move downstream in the plume region, the EEDF is shifting to the right. Therefore, we have an increased fraction of the electron population that have become energetic enough to exceed the electrostatic potential barrier and can leave the thruster potential well. Figures 8, 9, and 10 are a clear proof of the anisotropic electron dynamics taking place inside the thruster, and how this anisotropy is smoothed to generate a fast electron population leaving the thruster.
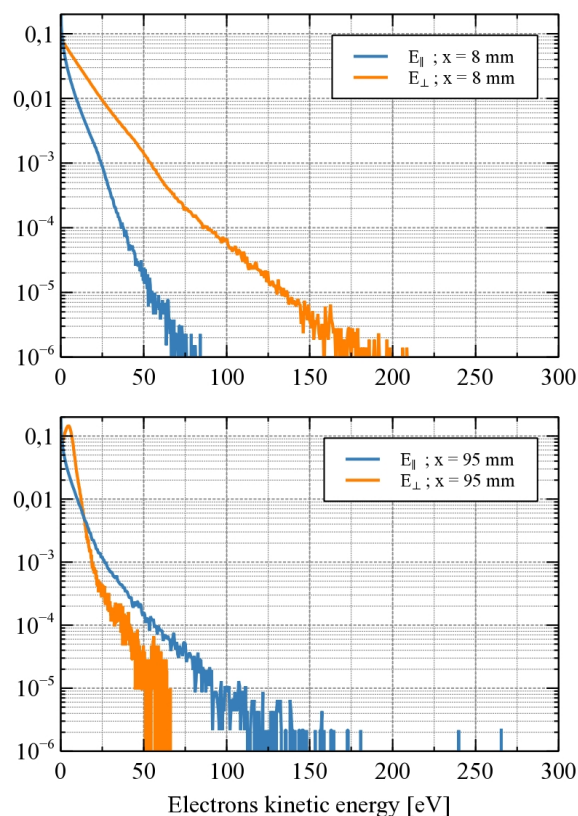

Figure 10. Perpendicular and parallel EEDF at two locations. Upper graph : in the source. Lower graph: close to the domain outlet.

C.   Parametric analysis

The previously presented results will constitute the baseline configuration for a simple parametric analysis. The baseline configuration, described in Table 1, was modified to generate three different new configurations to simulate, as shown in Table 2.

Table 2. Parametric study

Case	Description	Parameter
1	Reduced density of neutral particles.	$n_0 = 1 \times 10^{21} \, \mathrm{m}^{-3}$
2	ECR surface position closer to the backplate. x_{ECR} changed from 5 mm to 3 mm	$f_{EM} = 2.6 \, \mathrm{GHz}$
3	Increased cross-sectional area of the magnetic tube.	$A_0 = 2 \, \mathrm{cm}^2$

Regarding the electrons response in this parametric study, Fig. 11 shows the mean electron kinetic energy in both directions. We notice that for all cases the electron population is more energetic. For each simulation, it is possible to identify the ECR surface with the peak in perpendicular energy. The broader secondary peak in perpendicular energy inside the plasma source, as identified in section B, can also be noticed. It can be seen more clearly for the perpendicular energy of case 2 where its value at the end of the plasma source (x = 20 mm) is greater than the one reached at the ECR surface x = 3 mm. The increased longitudinal energy has a direct impact on the ion acceleration. Figure 12 shows a more energetic ion population for each of the simulated cases in comparison with the baseline configuration. Nevertheless, an increased ion energy was not the only result of the modified parameters. The ion current was also changed as can be seen in Fig. 13. This two variations can also be linked to the thrust force produced by the ions leaving the coaxial chamber. The thrust is proportional to the ions flux and to its kinetic energy. For case 1 and case 3, the thrust was increased because both parameters also increased as seen in the figures below. However, for case 2, the increased ion energy visible in Fig. 12 was counteracted by the ion flux decrease as shown in Fig. 13, leading to a negligible thrust modification.
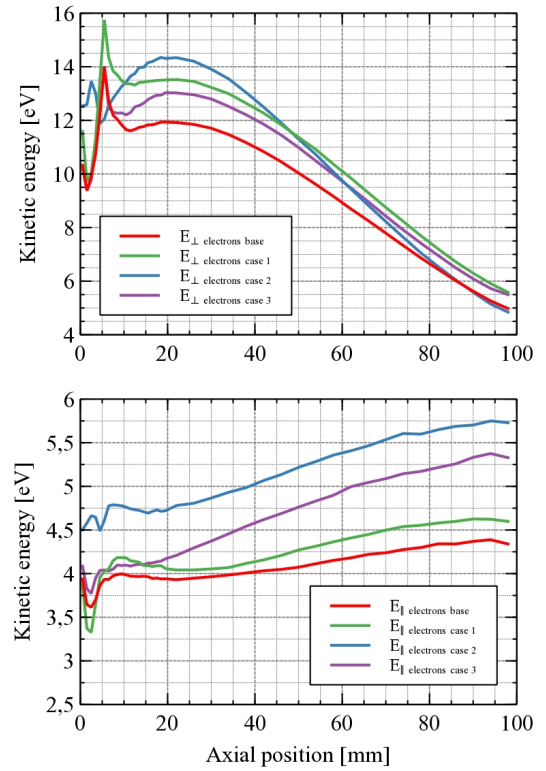

Figure 11. Electron mean kinetic energy. The graph at the top of the figure represents the perpendicular energy, and the other one the energy in the longitudinal direction.
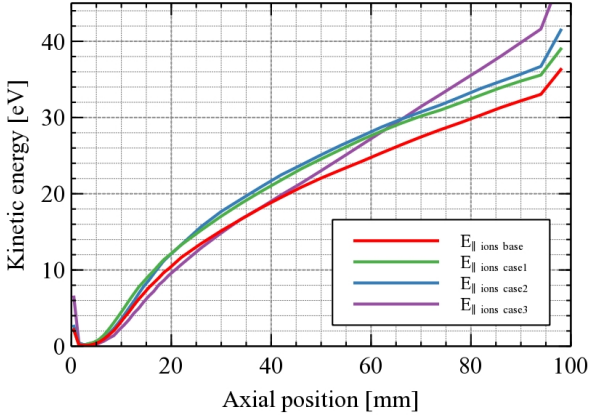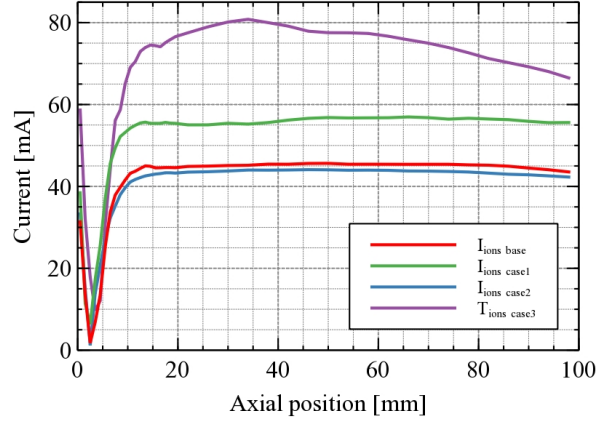
Figure 12. Ion mean kinetic energies.

Figure 13. Ion currents.

Until now we have been presenting the mean values of the energies for electrons and ions. But for the purpose of getting a better understanding of the phenomena taking place in each configuration, the following figures have proven to be extremely helpful. Figure 14 shows the perpendicular electron energy distribution function at different positions of the computational domain for each simulation.
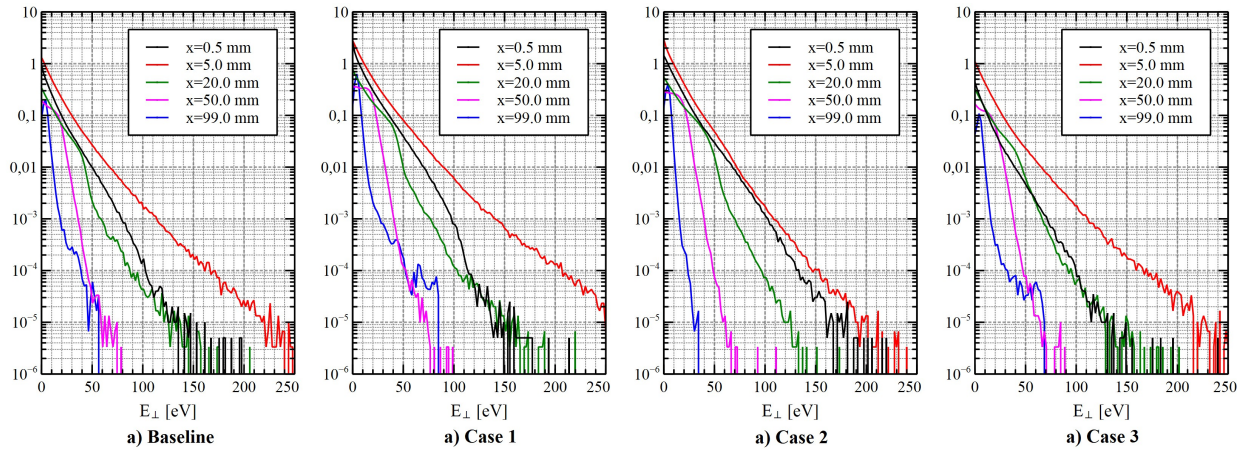

Figure 14. Electron energy distribution functions at different locations.

Figure 15 shows the electrons energy distribution contours over the whole domain for the perpendicular and longitudinal direction. The colormap represents the number of electrons at each energy level. We can notice the energy boost that the electrons receive in their perpendicular kinetic energy at the ECR surface. Having this information in mind, a few elements can be pointed out as possible explanations to the results presented in the previous section for each simulated configuration:

- **Case 1. Reduced density of neutral particles:** A reduced density of neutral particles would increase the mean time between collisions and, as a consequence, reduce the losses from the inelastic and ionization collisions. It leaded to higher energy values of the particles as shown in figures 11 and 12. This fact was already identified in Ref. 11. Figure 15 also illustrates this consequence. A comparison between the baseline configuration in Fig. 15a) and the case 1 in Fig. 15b), reveals that there is an increased concentration of electrons at higher energy levels in case 1 than in the baseline for any given point in the domain. The width of perpendicular energy distribution at x= 5 mm is around 30 eV for the baseline configuration and around 50 eV for case 1. Therefore, we have a better heating and as a result a more energetic electron beam in the longitudinal direction where the red stripe for case 1 has an energy width of around 5 eV greater than the one in Fig. 15a).

  This result is consistent with the experimental results presented in Ref. 9. Jarrige et al. used the
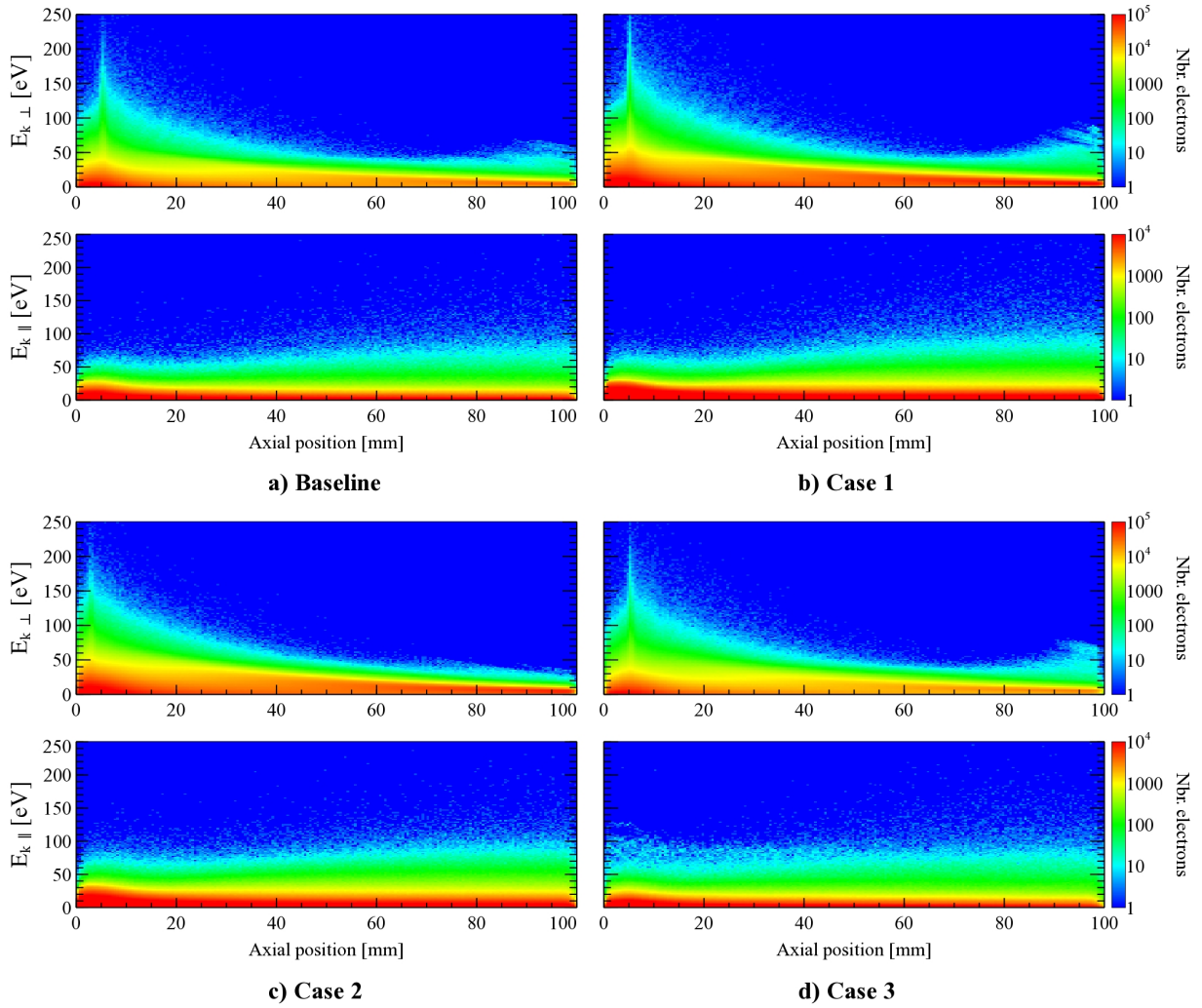
Figure 15. Electron energy distribution contour for each configuration. The graph at the top of each subfigure represents the perpendicular energy, and the other one the axial direction.

Laser-induced fluorescence (LIF) technique to study the ions acceleration in the magnetic nozzle of the ECRA thruster. The mean ion velocity was measured for different xenon flow rates and the results indicated an inverse correlation between these two parameters. Therefore, obtaining a more energetic ion population for a low density of neutral particles. Another result presented by Jarrige et al. was the inverse relationship between the xenon flow rate and the plasma potential in the magnetic nozzle. The exact values of our simulations can not be compared against this experimental data, but our results show the same tendency as we can see in Fig. 16 with an increased plasma potential for the reduced density of neutral particles in case 1.
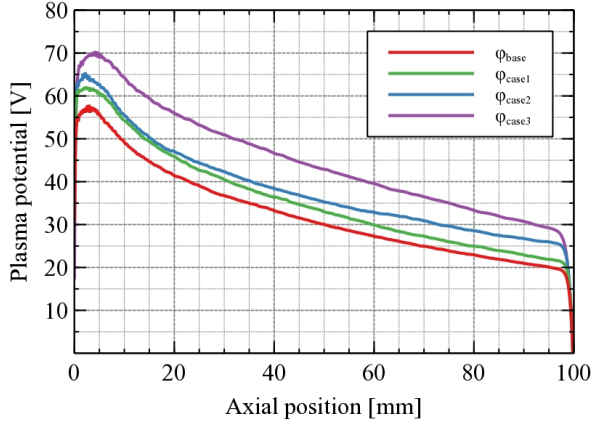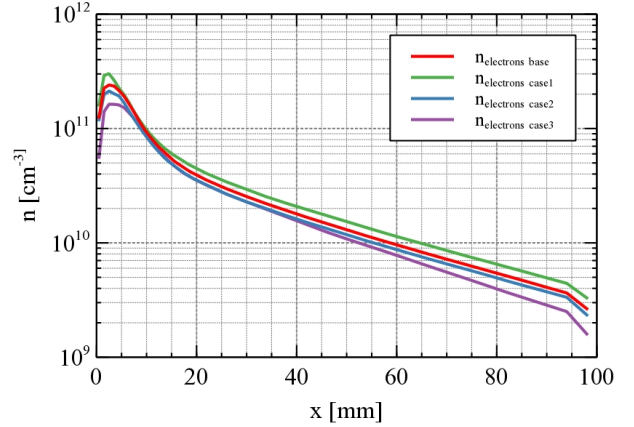

Figure 16. Plasma potential profiles.

Figure 17. Density distributions.

- **Case 2. ECR surface position closer to the backplate:** The total thrust gain obtained with this configuration is around 1.5%. Such a small variation may be considered negligible. The experimental results presented in Ref. 21 show the same conclusion. After varying the ECR surface position up to 4 mm from the backplate, the total thrust showed little sensitivity to these modifications.

  Nevertheless, it is interesting to highlight the fact that Fig. 12 shows an increased ion kinetic energy in the axial direction. It is actually an expected result since when the ECR surface get closer to the backplate, it means that the heating resonance condition is met upstream in the plasma source so the electrons have now a longer path before leaving the coaxial chamber. An argument to support this explanation comes from Fig. 15c). If we look at the electron longitudinal energy inside the coaxial chamber ($L < 20$ mm), we can notice an increased number of particles in comparison with the baseline configuration (specially those inside the green part).

  Another important fact to point out is that the maximum perpendicular energy reached by the electrons in Fig. 11 is lower than the value for the baseline configuration. The reason for this is that in case 2, the ECR surface is located in a region with a higher density of neutral particles causing energy losses in the electrons cyclotron motion. It is still unknown why this perpendicular energy keeps rising until exceeding the value at the ECR surface.

- **Case 3. Increased cross-sectional area of the magnetic tube:** The particles energy gain of this simulation may be explained by reduced wall losses. In our numerical model, a greater cross-sectional surface inside the coaxial chamber represents a better electron confinement and fewer wall losses.

As a final note, it is important to mention that the simulations carried out for this study were not the subject of a parametric optimization in order to match precisely the experimental tests. As a consequence, this simulations were compared to some previous experimental results only to identify trends and confirm or disprove hypothesis about what may be the thruster response when facing different operational conditions.

IV.   Conclusion

A simplified quasi-one-dimensional 1D3V (one-dimensional in space and three-dimensional in velocity) model has been developed and simulated using an electromagnetic PIC/MCC code. The code has a Maxwell

solver module to simulate the microwaves propagation inside the plasma. This feature provides an accurate description of the heating process for the electrons on the plasma source thanks to the cyclotron resonance phenomenon.

This model was used to get a better understanding of the particles dynamics inside the thruster. It also gave us some insight into the thruster response to a parametric study of several factors such as the ECR surface position, the background pressure, and its cross-sectional area. The results show the same trends obtained in previous experimental campaigns. This tendencies are: little sensitivity to the ECR surface location, and a reduced thruster performance as the background pressure is increased. The fact that our numerical simulations pointed out into the same direction as the experimental data is an encouraging result. Its a validation of our electromagnetic PIC/MCC code and give us confidence that the numerical models in our code can accurately reproduce the complex physics taking place inside the thruster.

This simplified model will continue to be exploited to get a deeper understanding of the heating process as the electromagnetic power is coupled into the plasma in the ECR zone. It will be the subject of forthcoming studies. Finally, this model will also guide future developments to get EM-PIC simulations in 2D and 3D.

Acknowledgments

References

[1] Mikellides, I. G., Katz, I., Hofer, R. R., Goebel, D. M., De Grys, K. H., and Mathers, A., "Magnetic Shielding of the Acceleration Channel in a Long-Life Hall Thruster," Physics of Plasmas 18, 033501 (2011).

[2] Dubois, L., Gaboriau, F., Liard, L., Harribey, D., Henaux, C., Boeuf, J. P., Mazouffre, S., and Boniface, C. Ion Acceleration through a Magnetic Barrier Toward an Optimized Double-Stage Hall Thruster Concept. Internationl Electric Propulsion Conference, 2017, pp. 110.

[3] ASD-Eurospace. Space Trends 2015. Global Activity Overview, Vol. 4th edition, 2015.

[4] Cannat, F., Lafleur, T., Jarrige, J., Chabert, P., Elias, P., and Packan, D. Optimization of a Coaxial Electron Cyclotron Resonance Plasma Thruster with an Analytical Model. Physics of Plasmas, American Institute of Physics, 2015.

[5] Jarrige, J., Elias, P.-Q., and Packan, D. Performance Comparison of an ECR Plasma Thruster Using Argon and Xenon as Propellant Gas. Internationl Electric Propulsion Conference, 2013, p. 420.

[6] Vialis, T., Jarrige, J., and Packan, D. "Geometry Optimization and Effect of Gas Propellant in an Electron Cyclotron Resonance Plasma Thruster." Internationl Electric Propulsion Conference, 2017.

[7] Jarrige, J., Elias, P.-Q., Cannat, F., and Packan, D. "Characterization of a Coaxial ECR Plasma Thruster." 44th AIAA Plasmadynamics and Lasers Conference, 2013.

[8] Cannat, F. Caractrisation et Modlisation dun Propulseur Plasma Rsonance Cyclotronique Des lectrons. Ph.D. Dissertation, Ecole Polytechnique, 2016.

[9] Jarrige, J., Correyero, S., Elias, P.-Q., and Packan, D. Investigation on the Ion Velocity Distribution in the Magnetic Nozzle of an ECR Plasma Thruster Using LIF Measurements. Internationl Electric Propulsion Conference, 2017, pp. 110.

[10] Correyero, S., Merino, M., Elias, P. Q., Jarrige, J., Packan, D., and Ahedo, E. Characterization of Diamagnetism inside an ECR Thruster with a Diamagnetic Loop. Physics of Plasmas, Vol. 26, No. 5, 2019. doi:10.1063/1.5093980.

[11] Elias, P.-Q. "Advances in the Kinetic Simulation of Microwave Absorption in an ECR Thruster". Internationl Electric Propulsion Conference, 2017.

[12] Sanchez-Villar, A., and Merino, M. Advances in Wave-Plasma Modelling in ECR Thrusters. Space Propulsion Conference, 2018.

[13] Ueno, K., Mori, D., Takao, Y., Eriguchi, K., and Ono, K. "Particle-in-Cell Simulation of a Micro ECR Plasma Thruster". Internationl Electric Propulsion Conference, 2015.

[14] Takao, Y., Koizumi, H., Komurasaki, K., Eriguchi, K., and Ono, K. Three-Dimensional Particle-in-Cell Simulation of a Miniature Plasma Source for a Microwave Discharge Ion Thruster. Plasma Sources Science and Technology, Vol. 23.

[15] Roe, P. Linear Bicharacteristic Schemes Without Dissipation. SIAM J. SCI. COMPUT., 1998, pp. 123.

[16] C.K. Birdsall, A. . L. Plasma Physics via Computer Simulation. IOP Publishing, 1986.

[17] H. R. Skullerud : The stochastic computer simulation of ion motion in a gas subjected to a constant electric field. J. Phys. D : Appl. Phys., 1:15671568, 1968.

[18] John H. Beggs, N. On the Treatment of Electric and Magnetic Loss in the Linear Bicharacteristic Scheme for Electromagnetics. NASA/Goddard Space Flight Center, 2000.

[19] Nguyen, B. T., and Hutchinson, S. A. The Implementation of the Upwind Leapfrog Scheme for 3D Electromagnetic Scattering on Massively Parallel Computers. Sandia National Laboratories, 1995.

[20] Peterschmitt, S., Porto, J. C., Elias, P., and Packan, D. A Diffusion Model in Velocity Space to Describe the Electron Dynamics in an ECR Plasma Thruster with Magnetic Nozzle. 2019.

[21] Vialis, T. Développement dun Propulseur Plasma à Résonance Cyclotron Electronique Pour Les Satellites. Ph.D. Dissertation, Sorbonne Université, 2019.